RSC Advances

PAPER

View Article Online
View Journal | View Issue

Check for updates

Cite this: *RSC Adv.*, 2022, **12**, 26789

Received 25th May 2022
Accepted 28th August 2022

DOI: 10.1039/d2ra03285f

rsc.li/rsc-advances

Hydroxyapatite coating on an aluminum/bioplastic scaffold for bone tissue engineering

Oratai Jongprateep, *[ab] Nonthaporn Jitanukul,[a] Khotamy Saphongxay,[ab] Benjamon Petchareanmongkol,[a] Ampika Bansiddhi,[a] Apirat Laobuthee, [a] Amornrat Lertworasirikul[a] and Ratchatee Techapiesancharoenkij[ab]

Three-dimensional printing can produce scaffolds with shapes and dimensions tailored for practical clinical applications. Enhanced osteoconductivity of such scaffolds is generally desired. Hydroxyapatite (HA) is an inorganic ceramic that can be used to coat such scaffolds and to accelerate healing during the bone restoration process. In this study, HA-coated aluminum/bioplastic scaffolds were fabricated, and their structural characteristics and osteoconductivity were evaluated. Aluminum/bioplastic scaffolds were fabricated by three-dimensional printing, and HA slurries with solids loadings of 10–20 vol% were used for coating. As solids loadings increased, the thickness of the coating layers slightly increased, whereas pore sizes decreased. The average compressive strength was comparable to that of cancellous bone. Potential osteoconductivity was tested by simulated body fluid immersion for 28 days, and the formation of the HA phase on the surface along with a weight increase indicates the potential bioactivity of the samples.

1 Introduction

Bones are an important part of the human body: they support the rest of the body, are connected to muscles, protect organs and bone marrow, and store minerals such as calcium and phosphorus. Various bone diseases can occur, including spinal disc degeneration, scoliosis, osteoporosis, bone infection, tumors, congenital defects, and osteoarthritis.[1] Apart from diseases, bones can fracture because of high impact forces or stress. The self-healing abilities of bones may not be sufficient for severe fractures. Several techniques have been employed to heal bone fractures or promote bone regeneration. One such technique is bone tissue engineering (BTE), which uses bone scaffolds.[2] The fundamental requirements for the practical application of bone scaffolds include high porosity, nontoxicity, corrosion resistance, and high durability. In addition, the bone scaffold materials must be biocompatible so that they are not rejected and do not cause any undesirable effects when implanted. The materials should also have mechanical properties and strength similar to that of real human bones.[2–8]

Various materials have been employed for bone scaffolds and implants. Metals such as magnesium, zirconium, titanium, and stainless steel are commonly used in implants because of their high strength, ease of forming, and low toxicity.[3,8] Titanium alloy is a well-known biomaterial that is widely used as a bone replacement, to which magnesium, nickel, cobalt, and/or chromium are added to enhance strength, flexibility, and malleability.[12–16] Moghaddam *et al.*[13] reported that adding vanadium and aluminum to titanium can also improve strength and corrosion resistance. The Ti–6Al–4V alloy is one of the most commonly used materials in medical devices owing to its good mechanical properties, corrosion resistance, and low cost.[17,18] In addition to being a component of robust titanium alloys, aluminum is extensively used as a major component in medical devices due to its strength, durability, flexibility, lightweight, corrosion resistance, recyclability, and abundance.[19] To achieve low potential for severe toxicity and to attain good biocompatibility with the human body, surface-treated aluminium alloy is used in biomedical applications.[20–22]

Processing the material to obtain the required shape is also important. Numerous material processing techniques such as casting and powder metallurgy are available. However, these techniques require the utilization of molds, which have high tool costs. Three-dimensional (3D) printing is capable of fabricating near-net-shape samples without a mold as well as unique and customized parts. This technique can also produce small parts or specific details, so it is suitable for producing bone scaffolds.[23,24]

Despite the desirable mechanical properties of metals or alloys, their application in implants has several drawbacks. Metal implants have low osteoconductivity, which slows the healing process. Numerous studies have reported the corrosion of implants over time.[3,9–11] Metals are also toxic in high doses.[25]

---

[a] *Department of Materials Engineering, Faculty of Engineering, Kasetsart University, Bangkok 10900, Thailand. E-mail: fengotj@ku.ac.th*

[b] *ICE-Matter Consortium, ASEAN University Network/Southeast Asia Engineering Education Development Network (AUN/SEED Net), Bangkok, Thailand*

Metal ion leaching may cause harmful conditions to human body. For example, excessively high content of aluminium in human blood can induce problems in internal organ such as kidney, lung, liver, and bone.[26–28] It has been reported that the majority of aluminium intake from food, medicine, and medical implants is eliminated through urine excretion. The high level of remaining aluminium ions, however, can result in chronic renal disease,[28] inflammation of lung, intestine, heart, and testis, as well as weakened immunity system.[29–32] High content of aluminium ions also induces the risk of triggering neurodegenerative diseases, including Alzheimer's disease and Parkinson's disease, and multiple sclerosis.[33–35]

While aluminium toxicity is not coverable, many of the above drawbacks can be prevented by coating the implant with biocompatible materials. Hydroxyapatite (HA) ($Ca_{10}(OH)_2(PO_4)_6$) is an inorganic ceramic that is used in BTE owing to its chemical composition similar to that of bones, high osteoinductivity and osteoconductivity, and excellent biocompatibility.[36–42] However, its relatively low strength has limited the application of HA as a bone substitute.[43,44] An effective option for producing a high-strength bone restoration material with enhanced osteoconductivity is to coat a metal or alloy implant with HA. Coating a metal implant with HA promotes bone growth, strengthens the bond between the metal and bone tissue, accelerates healing and bone restoration,[45] and improves osteoconductivity and corrosion resistance.[46,47] The ion reaction between HA and body fluid can result in bone regeneration.[48,49] HA coating can be achieved by various techniques, including the sol–gel method, electrophoresis, thermal spray technique, chemical vapor deposition, and ion beam sputtering. The hydrothermal technique offers advantages such as low processing temperature and short processing time.[50]

In this study, simple and robust processing techniques were combined to fabricate bone scaffolds and coat them with HA. The study had three main parts: 3D printing of aluminum/bioplastic scaffolds, synthesis of HA powder by solution combustion, and coating the scaffolds with HA by the hydrothermal technique. The chemical composition and microstructure of the synthesized HA powder were examined, and the properties of the coated scaffolds were evaluated in terms of strength and potential bioactivity.

2 Experimental

2.1 Sample preparation

2.1.1 Scaffolds. A commercially available aluminum/polymer composite filament (Virtual Foundry, China) with a diameter of 1.75 mm was used for 3D printing. Specifically, the fused deposition modeling technique was used. The scaffolds were designed as cubic-shaped samples with dimensions of 20 mm × 20 mm × 20 mm. To create voids that imitate the porous structure of human bones, linear grids with a spacing of 2 mm × 2 mm were selected as the infill pattern. Fig. 1 shows an example of a 3D-printed scaffold, and Fig. 2 shows the materials and equipment used.

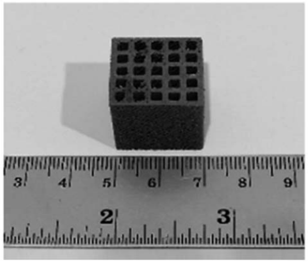

Fig. 1 3D-printed scaffold.

Fig. 2 3D printer and filament used to fabricate the scaffold.

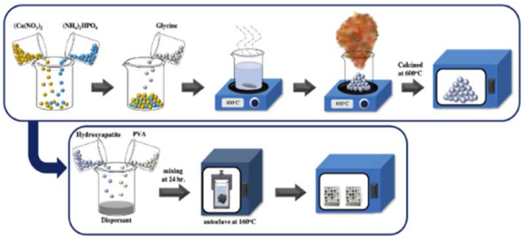

Fig. 3 HA synthesis by solution combustion.

2.1.2 Coating powder. Fig. 3 shows the solution combustion technique used to synthesize HA powder. An aqueous solution containing calcium nitrate tetrahydrate ($Ca(NO_3)_2\cdot 4(H_2O)$, Daejung, 97.0%) and ammonium phosphate dibasic ($(NH_4)_2\cdot HPO_4$, Daejung, 98.5%) with a Ca : P molar ratio of 2.3 : 1 was prepared. Glycine, which acted as the combustion fuel, was added to the prepared solution to obtain an aqueous solution with a Ca : P : glycine molar ratio of 2.3 : 1 : 1.9. Combustion reaction was initiated when the prepared solution was heated at 400 °C for approximately 1 h. Upon the completion of the combustion reaction, the synthesized powder was collected and calcined at 600 °C for 3 h.

2.2 Coating procedure

The hydrothermal process was used to coat the scaffolds with HA. The synthesized HA powder, polyvinyl alcohol ($(–CH_2–CH(OH)–)_n$, 1500, Daejung), and dispersant (Darvan 821/D821A6) were mixed with deionized water to prepare slurries with solids loadings of 10, 15, and 20 vol% HA. The scaffolds were then immersed into the HA slurry, which was heated at 160 °C for 5 h. Then, the scaffolds were calcined at 600 °C for 3 h.

2.3 Characterization

2.3.1 Scaffolds prior to coating. The phase identification of the scaffolds was conducted using an X-ray diffractometer (XRD, Bruker, D8 Advance) over a 2-theta angle range of 30–80° at a step size of 0.09°. An energy-dispersive X-ray spectrometer (EDS, Hitachi, SU3500) was employed for elemental analysis and elemental mapping. A Fourier transform infrared spectrometer (FTIR, Bruker, Alpha) was used to characterize the polymeric component in the filament. Differential scanning calorimetry (DSC, Mettler Toledo, DSC 1 Module) and thermogravimetric analysis (TGA) were employed to evaluate the thermal characteristics of the polymer. A scanning electron microscope (SEM, Hitachi, SU3500) was used to observe the microstructure.

2.3.2 Coating powder. The chemical composition of the synthesized powder was analyzed by XRD (Bruker, D8 Advance), the microstructure was observed by SEM (Hitachi, SU3500), whereas the particle size distributions was examined by Laser Scattering Particle Size Distribution Analyzer (HORIBA, LA960).

2.3.3 Coated scaffolds. XRD (Bruker, D8 Advance) and EDS (Hitachi, SU3500) were used to test the phase and chemical composition, respectively, of the coated scaffolds. SEM (Hitachi, SU3500) was used to observe the microstructure. ImageJ and Origin Pro8.5 software were employed to determine the pore size and porosity of the coated scaffolds. A universal testing machine (Hounsfield, H50KS) was used to measure the compressive strength of the coated scaffolds. Compressive strength was calculated from the applied load divided by the cross-sectional area of the samples. Statistical analysis, specifically assessment of the statistical significance, was performed on the compressive strength values of the uncoated and coated scaffolds using Microsoft Excel. Two-parameter Weibull distribution analysis was performed to evaluate the reliability of the uncoated and coated scaffolds. Bioactivity was evaluated in terms of the change in the weight of samples after immersion in simulated body fluid (SBF) for 28 days.

3 Results and discussion

3.1 Characteristics of uncoated scaffolds

3.1.1 Microstructure. Fig. 4 shows a scanning electron micrograph of the scaffold microstructure. A rough surface with segregated particles can be observed after heating at 600 °C for 3 hours. Evidence of unconnected particles might be attributed to removal of binder and organic compounds during the heat treatment. This binder burnout process created voids and unbound particles, leading to lower packing density and consequently lower mechanical strength of the scaffold.[51]

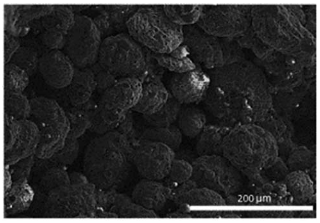

Fig. 4 Scanning electron micrograph of the scaffold microstructure.

3.1.2 Composition. Fig. 5 shows the XRD results for the scaffolds. At scanning angles of 30–90°, a single phase of aluminum (JCDPS 03-065-2869) was observed. Fig. 6 shows the elemental mapping by EDS, which also confirmed the presence and uniform distribution of aluminum in the scaffolds.

Table 1 presents the EDS results for the scaffold composition. The scaffolds mainly consisted of aluminum and had a composition of 38.9 at% aluminum, 28.2 at% oxygen, and 32.9 at% carbon. The high carbon content was attributed to the high polymeric binder content in the composite filament.

Because the scaffold was fabricated from a commercially available composite filament consisting of aluminum and polymeric material, the polymeric binder needed to be identified. Fig. 7 shows the FTIR spectrum of the scaffold. The characteristic absorption bands of the peaks observed at 3440, 2956, 1733, 1440, and 1148 cm^{-1} correspond to the –OH(COOH), –CH$_3$(S), –C=O, –CH$_3$(B), and –C–O(COOH) functional groups, which are commonly observed in polylactic acid (PLA).[52,53]

Thermogravimetric analysis (TGA) was employed to determine the volatile components, specifically the polymeric binder in the filament, according to the change in weight. As the sample was heated from room temperature to 500 °C, a noticeable loss in mass occurred at 225–400 °C, as shown in Fig. 8(a).

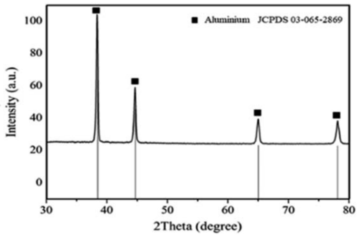

Fig. 5 XRD pattern of the scaffold.

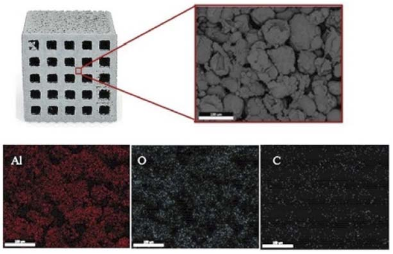

Fig. 6 Elemental mapping of the scaffold.

Table 1 Elemental composition of uncoated scaffolds

Element	Composition (at%)
Al	38.86
O	28.17
C	32.97

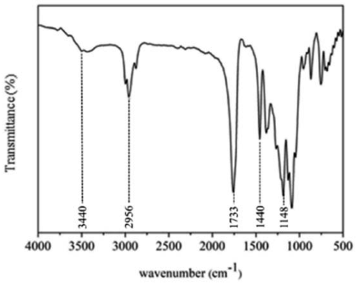

Fig. 7 Fourier transform infrared spectrum of the scaffold.

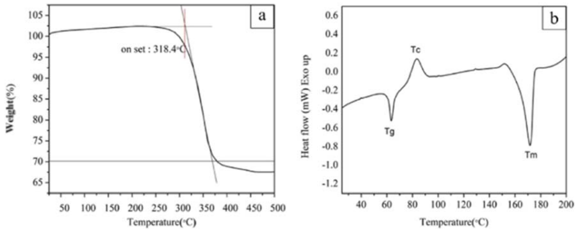

Fig. 8 Thermal analysis of the bone scaffold: (a) TGA curve and (b) DSC curve.

The extrapolated onset temperature corresponding to the degradation of the polymeric binder was 318.4 °C. This is close to the degradation temperature for PLA, which has been reported to be 300–372 °C. The TGA results agree with the study which indicates that the polymeric binder in the filament mainly comprised PLA.[54–56]

DSC measures the temperatures and heat flows associated with transitions in materials, and it was employed for thermal analysis of the scaffolds. The DSC curves exhibited prominent endothermic signals close to 58 °C and 170 °C, as shown in Fig. 8(b). These signals may represent the glass transition temperature (T_g) and melting temperature (T_m), respectively, of the polymeric component. An exothermic signal representing the crystallization temperature (T_c) was clearly observed close to 83 °C. The DSC results agreed with the FTIR and TGA results.

PLA is a biocompatible polymer extensively used in medical applications, including implants or bone scaffolds, owing to its biodegradability, nontoxicity, and environmental friendliness.[57–60] Da Silva *et al.*[61] noted that PLA can degrade in the human body and can be excreted in the urine and during breathing.

3.2 Characteristics of the coating powder

3.2.1 Chemical composition. The phases of the Ca–P compound synthesized the by solution combustion technique were identified by XRD. Fig. 9 shows that the synthesized powder had peaks corresponding to HA (JCPDS 01-084-1998) at scanning angles of 30–90°. No evidence of a secondary phase was detected. These results indicate that single-phase HA was successfully obtained by solution combustion.

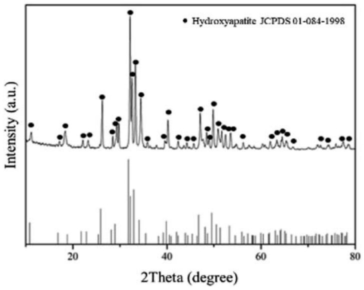

Fig. 9 X-ray diffraction pattern of HA powder synthesized by solution combustion.

3.2.2 Microstructure. SEM was employed to observe the size and morphology of the HA particles. Fig. 10(a) and (b) shows equiaxed and slightly elongated particles with an average size of 170.0 ± 51.9 nm. Nevertheless, some particles agglomerate into clusters with an average size of 10.0 ± 5.9 μm, as shown in Fig. 10(c). Attributed to high surface energy and large surface area, fine particles of hydroxyapatite are inclined to be agglomerated.[49]

The coating particle size can affect the characteristics of the scaffold. For biomedical applications, finer HA particles are preferred because of the high surface area. That could enhance interaction between HA and scaffold. According to Hu *et al.* and Christian *et al.*, bioactivities of the calcium phosphate are associated with size of the particles. Fine particle sizes provide large active surface area and nucleation sites for formation of apatite layer, promoting cell proliferation and osteoconductivity.[62–66]

3.2.3 Particle size distribution. In the previous section, an image analysis was employed in estimation of particle sizes of the synthesized HA powder. In this section, particle size distribution was examined to confirm the image analysis. According to the results from the laser scattering particle size

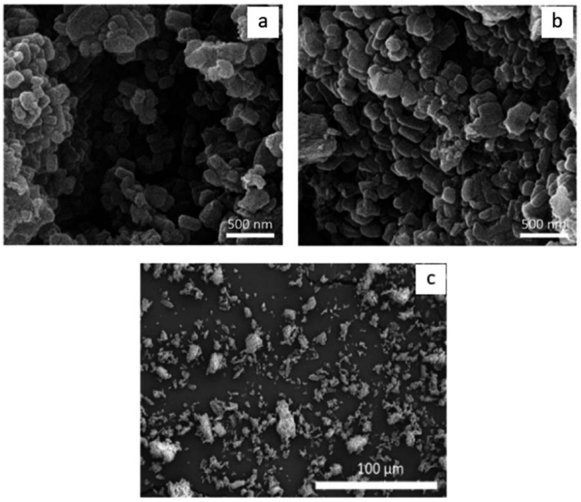

Fig. 10 (a) and (b) Scanning electron micrographs showing the morphology of HA particle. (c) Scanning electron micrographs showing agglomeration of HA particles into clusters.

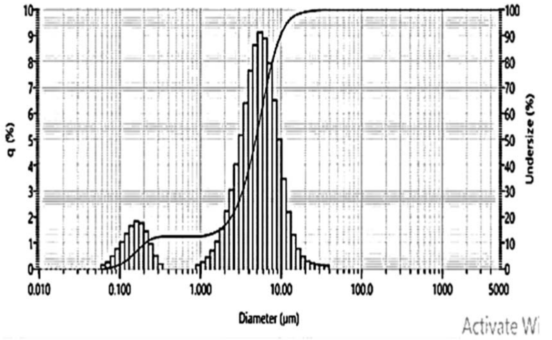

Fig. 11 Particle size distributions of HA particles.

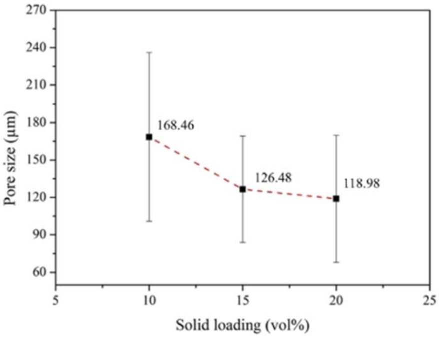

Fig. 14 Average pore sizes of the coated scaffolds analyzed by ImageJ.

distribution analyzer, as shown in Fig. 11, bimodal particle size distribution is evident. The first peak of the bimodal particle size distribution represented primary particles with the majority of sizes in the range between 150–200 nanometers, whereas the second peaks represented flocculated clusters with the majority of sizes ranging from 4–7 μm.

3.3 Characteristics of the coated scaffolds

3.3.1 Microstructure. SEM was also employed for the microstructural analysis of the coated scaffolds. Fig. 12 shows that the coated scaffolds had a flower-like morphology. Similar observations were reported by Ciobanu *et al.*[67]

To enhance osteoconductivity, a proper pore structure for the HA coating is required. A pore size of 50–500 μm is considered appropriate for practical applications.[68,69] Fig. 13 shows the scanning electron micrographs of the pore structures of the coated scaffolds. ImageJ was employed to analyze the pore size. The results indicated that increasing the solids loadings of HA reduced the pore size. Fig. 14 shows that scaffolds coated by 10, 15, and 20 vol% HA had average pore sizes of 168.46 ± 67.60, 126.49 ± 42.67, and 118.98 ± 50.85 μm, respectively. According to Won *et al.*,[70] scaffolds with pore sizes of 100–325 μm are optimal for BTE.

In addition to the pore size, porosity affects the development of tissue and blood vessels as well as compressive strength.[71] ImageJ and Origin Pro8.5 were employed to analyze the porosity of the coated scaffolds. Fig. 15 shows that the average porosities of the scaffolds coated by 10, 15, and 20 vol% HA were 69.48% ± 2.00%, 66.73% ± 4.61%, and 64.40% ± 2.97%, respectively. These values are comparable to those reported by other researchers and are suitable for practical application. According to Kim *et al.*,[72] bone scaffolds with a structure similar to cancellous bone should have a porosity of 50%–90%.

Fig. 16 shows the chemical compositions of the coated scaffolds according to EDS. Elemental mapping was conducted

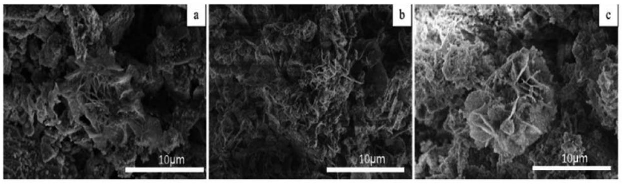

Fig. 12 Scanning electron micrographs showing the microstructure of scaffolds coated by (a) 10, (b) 15, and (c) 20 vol% HA.

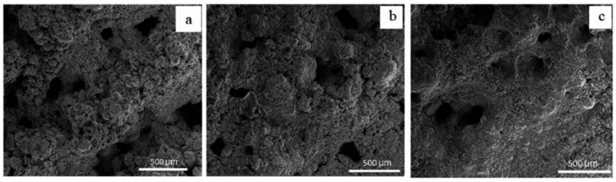

Fig. 13 Scanning electron micrographs showing the pore structure of scaffolds coated by (a) 10, (b) 15, and (c) 20 vol% HA.

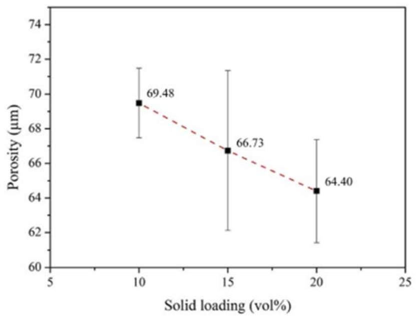

Fig. 15 Average porosity of scaffolds coated by HA analyzed by ImageJ and Origin Pro8.5.

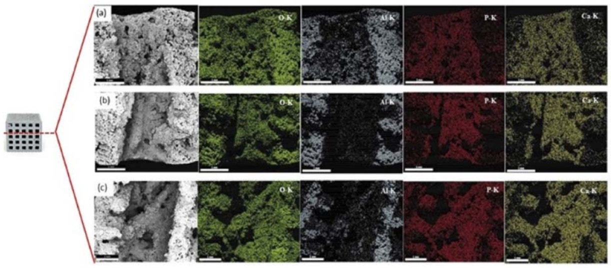

Fig. 16 Scanning electron micrographs, EDS spectrum, and elemental mapping of the scaffolds coated by (a) 10, (b) 15, and (c) 20 vol% HA.

Table 2 Elemental compositions of coated scaffolds according to solids loading

Element	Chemical composition (at%) 10 vol% HA	15 vol% HA	20 vol% HA
Ca	17.605 ± 0.70	23.59 ± 1.34	26.29 ± 2.57
P	6.25 ± 0.32	9.09 ± 0.56	9.18 ± 0.15
O	59.20 ± 0.27	55.47 ± 0.31	56.07 ± 1.09
Al	18.29 ± 0.61	11.84 ± 1.59	8.45 ± 1.32
Ca/Al	0.96 ± 0.005	2.01 ± 0.38	3.17 ± 0.80

to examine the distribution of the elements on the scaffold surface. All elements had a fairly uniform distribution. Table 2 presents the quantitative analysis of the key elements: Ca, P, Al, and O. The Ca/Al ratio differed significantly according to solids loadings: with the lowest and the highest in the samples coated with 10 and 20 vol% HA, respectively. It is generally accepted that the elemental composition values obtained from the EDS analysis rely on interactions of X-ray and the sample. Therefore, if the HA coating layer is uniform, non-porous and thick, aluminium signal may not be detected. Nevertheless, since the HA coating layers in this study demonstrated highly porous structure, X-ray could penetrate to aluminium surface through pores.

For the samples coated with 10 vol% HA, the largest pore sizes, the highest porosity and thinner HA coating layer were evident. On the contrary, thicker coating layer with finer pores and reduced porosity was observed in the samples coated with 20 vol% HA. For the coated scaffold with HA at higher solids loading, finer pore size and lower porosity suppress aluminum signal in the EDS spectrum, resulting in the enhanced Ca/Al ratio.

3.3.2 Thickness of the coating layers. The uniformity and thickness of the coating affect its adhesion to and strength of the underlying structure. Fig. 17 shows scanning electron micrographs of the coating thickness, which increased with solids loading. Fig. 18 shows the average thicknesses of coated scaffold with 10, 15, and 20 vol% HA. When the scaffold thickness is excluded, the thickness of the HA coating layers were 38.21 ± 17.58, 42.65 ± 28.47, and 46.53 ± 29.68 μm, respectively. These values are comparable to those in the literature.[72–74] Converse *et al.*[73] obtained an HA coating thickness of 42–89 μm and reported a decrease in porosity with increasing HA content. The scanning electron micrographs also showed greater nonuniformity as solids loading increased. Thus, the optimal microstructure was achieved for a scaffold coated with 10 vol% HA.

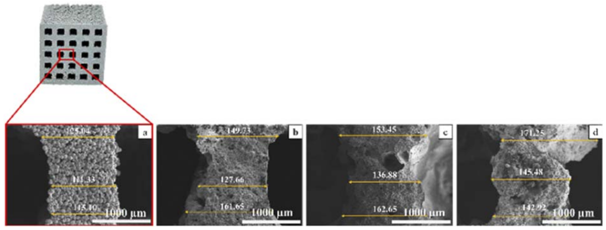

Fig. 17 Scanning electron micrographs showing thickness of the (a) uncoated sample, coated with (b) 10 vol% solids loading, (c) 15 vol% solids loading, and (d) 20 vol% solids loading.

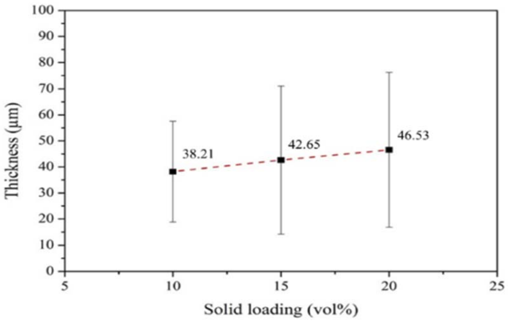

Fig. 18 Thickness of the coating layer on the scaffold according to solids loading.

3.3.3 Compressive strength. A key requirement for bone scaffolds is acceptable compressive strength. Table 3 indicates that the uncoated scaffolds exhibited exceptionally low strength, which may be attributable to the unconnected grains shown in Fig. 4. The coated scaffolds demonstrated compressive strength that was acceptable for human bones. Cancellous bone has a strength value of 0.1–16 MPa, and the coated scaffolds had an average compressive strength value of 0.84–2.98 MPa. The scaffolds coated by 10 vol% HA exhibited the greatest average strength of 2.98 MPa, and the scaffolds coated by 20 vol% HA demonstrated the minimum strength of 0.23 MPa. Statistical significance of compressive strength of the uncoated and coated scaffold was evaluated. The values of $p < 0.001$ (designated as *** in Fig. 19) were obtained. With very low p values, very high significance was demonstrated.[75]

The low average compressive strength in the samples the high solids loading may be attributed to the nonuniformity and excessive thickness of the coating. As shown in Fig. 19, the samples coated with 20 vol% HA revealed the greatest standard deviation compared to its mean compressive strength. The coefficient of variation (the ratio between standard deviation of dataset and the mean of dataset) of the samples is 0.5, indicating that the compressive strength values of the samples are relatively scattered. The dispersion of the strength values might be associated with nonuniform coating. As shown in Fig. 20, the scanning electron micrographs of the samples coated with 10 vol% HA reveal thinner coating layer with relatively uniform thickness. On the contrary, thicker but nonuniform coating layers were observed in the sample coated the 15 and 20 vol% HA.

Schmidmaier *et al.*[74] reported that a thick coating layer may be at a higher risk of detachment from the implant. Thus, a high solids loading may result in a nonuniform coating with poor adhesion and compressive strength.[76]

3.3.4 Weibull distribution analysis and reliability of bone scaffold samples. Since the compressive strength results with highly scattered data were obtained, the Weibull analysis was further performed for prediction the reliability of the bone

Table 3 Compressive strength of coated scaffolds

	Compressive strength (MPa)			
Sample no.	Uncoated	Coated with 10 vol% HA	Coated with 15 vol% HA	Coated with 20 vol% HA
1	0.15	2.26	1.50	0.23
2	0.18	2.57	1.83	0.37
3	0.19	2.91	1.91	0.73
4	0.20	2.99	2.04	0.75
5	0.23	3.12	2.15	0.77
6	0.24	3.22	2.23	1.13
7	0.25	3.30	2.35	1.31
8	0.35	3.48	3.01	1.41
Average	0.22	2.98	2.13	0.84
Standard deviation	0.06	0.40	0.44	0.42

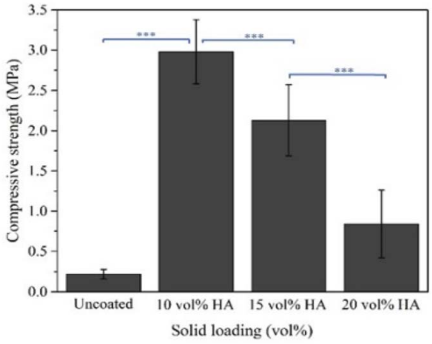

Fig. 19 Compressive strength of uncoated and coated scaffolds.

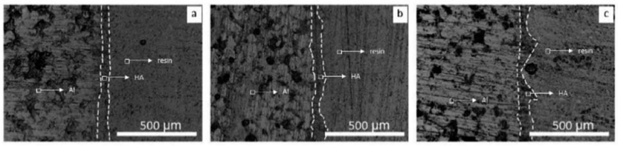

Fig. 20 Scanning electron micrographs showing the sample coated with (a) 10 vol% solids loading, (b) 15 vol% solids loading, and (c) 20 vol% solids loading.

scaffold. Fig. 21 shows the Weibull plots obtained for the uncoated and coated scaffolds. Good linearity with a correlation coefficient (R^2) greater than 0.90 was obtained ($\ln(x)$ *vs.* $\ln(-\ln(1-F(x)))$). Table 4 presents the results of the reliability analysis on the probability that the scaffolds would meet bone strength requirements. Numerous studies have reported that cancellous bone has a compressive strength value of 0.1–16 MPa.[77] The reliability analysis revealed that the uncoated scaffolds did not achieve the required compressive strength, whereas the scaffold coated by 10 vol% HA exhibited the greatest compressive strength and achieved the minimum required compressive strength. The scaffold coated by 10 vol% HA demonstrated an excellent survival probability of 100% when subjected to stresses of 0.5–1.50 MPa. At stresses of 2 and 2.50 MPa, survival probability declined to 97% and 85%, respectively. For scaffolds coated with 15 vol% HA, a survival probability of 90% was achieved at a compressive stress of 1.5 MPa. However, the survival probability dropped substantially to 22% at a stress of 2.5 MPa. Scaffolds coated with 20 vol% HA had a low survival probability for a stress of 2.5 MPa. On the basis of the results for porosity, uniformity, and compressive strength, a solids loading of 10 vol% HA was concluded to obtain a coated scaffold with the best properties.

3.3.5 Bioactivity. Some of the key desirable characteristics of the bone scaffolds include biodegradability and bioactivity, which promote bone regeneration.[75]

The bioactivity of the coated scaffolds can be evaluated as a result of HA immersion into SBF for 28 days. During the course of SBF immersion, HA dissolves in SBF and release Ca^{2+} and PO_4^{3-}, which increased ion concentrations around the HA and provided favorable sites for apatite nucleation and crystallization. Through electrostatic attraction, negatively charged OH^- and PO_4^{3-} ions interact with positively charged Ca^{2+} ions, resulting in chemical bonding and formation of HA layer on the surface of the scaffold.[48,78–80]

Fig. 22 shows scanning electron micrographs of the scaffolds coated by HA slurries before and after SBF immersion. The

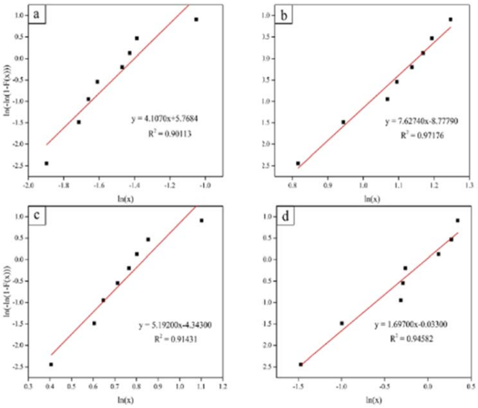

Fig. 21 Weibull plots for the compressive strength of scaffolds: (a) control, (b) coated with 10 vol% HA, (c) coated with 15 vol% HA, and (d) coated with 20 vol% HA.

Table 4 Reliability analysis of coated scaffolds

	Reliability			
Compressive strength (MPa)	Uncoated	Coated with 10 vol% HA	Coated with 15 vol% HA	Coated with 20 vol% HA
0.50	0.00	1.00	1.00	0.74
1.00	0.00	1.00	0.99	0.38
1.50	0.00	1.00	0.90	0.15
2.00	0.00	0.97	0.62	0.04
2.50	0.00	0.85	0.22	0.01
3.00	0.00	0.51	0.02	0.00
3.50	0.00	0.11	0.00	0.00
4.00	0.00	0.00	0.00	0.00
4.50	0.00	0.00	0.00	0.00
5.00	0.00	0.00	0.00	0.00

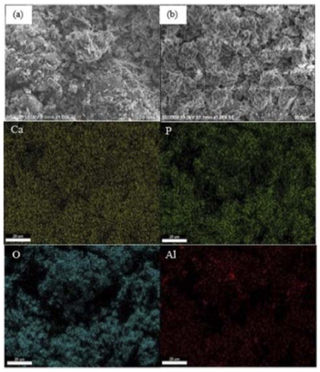

Fig. 22 Scanning electron micrographs and elemental mapping of the scaffolds coated by hydroxyapatite slurries with 10 vol% (a) before immersion in SBF, and (b) after immersion in SBF 28 days.

micrographs revealed porous morphology similar to that of HA, indicating potential bone growth with the HA coating. To ensure that the HA-like morphology did not belong to the existing HA coating layer, changes in weight after SBF immersion were used as indicators of bone-bonding ability. Table 5 demonstrates that the coated scaffolds increased in mass by more than 10% after immersion. This is similar to the observations of Chandra *et al.*,[81] who reported a mass of 5.93–6.79% after Fe-doped HA samples were immersed in SBF for 4 weeks.

The presence of HA was also confirmed by EDS. Elemental mapping of the coated scaffolds, as shown in Fig. 22 reveals a uniform distribution of elements on the surfaces. Table 6 presents a quantitative analysis of the key elements: Ca, P, Al, and O. The Ca/P ratios of 2.81 ± 0.21, 2.53 ± 0.09 and 2.90 ± 0.08 were evident in the samples coated by 10, 15, and 20 vol% HA, respectively. Elemental analysis of the samples prior to SBF immersion was previously shown in Table 2. The Ca/P ratios of 2.81 ± 0.03, 2.53 ± 0.01, and 2.86 ± 0.32 were observed in the samples coated by 10, 15, and 20 vol% HA, respectively. The Ca/P values of the HA coating after SBF immersion is close to that obtained prior to SBF immersion, indicating presence of HA after SBF immersion.

It should be addressed that non-stoichiometric apatite with the high value of Ca/P was obtained in this study. Stoichiometric HA has the Ca/P ratio of 1.67. Substantial variation of Ca/P ratio from the stoichiometric value can occur as a result of ion substitution. The loss of negative charges, which leads to the increase of Ca/P ratio, may occur when trivalent PO_4^{3+} ions in HA structure are substituted by bivalent ions such as carbonate. Carbonate substitution in HA can be represented by the following formula:

$$Ca_{10-x+u}(PO_4)_{6-x}(CO_3)_x(OH)_{2-x+2u} \text{ with } x \leq 2 \text{ and } u \leq x/2$$

It is noted that the hydroxyapatite powder used for coating was synthesized by the solution combustion technique, where carbon containing compound (glycine) was used as combustion fuel. Therefore, carbonate substitution can be possible. Average Ca/P ratios of the synthesized powder, coated layers (both before and after SBF immersion) were in a comparable range.

Table 5 Weight of coated scaffolds before and after immersion in SBF

HA (vol%)	Weight before SBF immersion (g)	Weight after SBF immersion (g)	Weight increase (%)
10	2.9065 ± 0.05	3.2849 ± 0.05	11.78
15	2.9942 ± 0.05	3.4032 ± 0.05	13.65
20	2.077 ± 0.05	2.3016 ± 0.05	10.81

Table 6 Quantitative element analysis of coated scaffolds after immersion in SBF for 28 days

	Chemical composition (at%)		
Element	10 vol% HA	15 vol% HA	20 vol% HA
Ca	8.195 ± 2.22	14.61 ± 0.20	20.41 ± 14.86
P	2.88 ± 0.57	5.78 ± 029	7.10 ± 5.32
O	69.65 ± 0.43	65.45 ± 0.70	64.48 ± 13.22
Al	19.26 ± 2.36	14.14 ± 1.2	7.69 ± 6.53
Ca/P	2.81 ± 0.21	2.53 ± 0.09	2.90 ± 0.08

Potential enhancement of bioactivity in ion-substituted HA may be associated with increase solubility. It is commonly accepted that HA is hardly soluble. Ion substitution potentially creates ionic vacancies, strains, and heterogeneity of composition, which destruct crystal cohesion and result in increased solubility. It has been reported that when the carbonate substitution increases, higher solubility product constant (K_{sp}) increases. Nucleation ability of HA is also related to supersaturation ratio which generally associates with high solubility.[82]

Another possible explanation for high Ca/P ratio involves formation of a hydrated surface layer. The existence of a hydrated layer, mainly containing bivalent ions such as Ca^{2+}, promotes spontaneous ion release and ion exchange. In addition, interfacial energy is potentially decreased, which accommodate the nucleation of HA.[66]

From the aforementioned discussion related to non-stoichiometric HA, it can be possibly deduced that high Ca/P ratio may be advantageous in terms of enhancement of bioactivity. A similar observation has been reported by Yang *et al.*, who states that the coating prepared by plasma electrolytic oxidation at different Ca/P ratios yields different bioactivity. Improvement of the bioactivity of the coated implant can be achieved with higher the Ca/P ratio.[83]

4 Conclusions

Aluminum/PLA scaffolds were successfully fabricated and coated with HA. The scaffold was 3D-printed, whereas a hydrothermal method was used for the HA coating. HA powder with an average particle size of <200 nm was synthesized by solution combustion and used for the coating process. The uncoated scaffolds showed a rough surface morphology with segregated grains of aluminum. By contrast, the coated scaffolds revealed a flower-like morphology. The pore size and thickness of the HA coating were affected by the solids loading of the HA slurry. An average pore size of 118.98–168.46 μm and coating thickness of 38.21–46.53 μm were observed for scaffolds coated with 10, 15, and 20 vol% HA. An average compressive strength value of 0.84–2.98 MPa was achieved. The optimal coating properties were obtained at 10 vol% HA. The coated scaffolds were then tested for reliability and potential bioactivity. The scaffolds coated with 10 vol% HA achieved 100% reliability when subjected to a compressive stress of 1.5 MPa. The mass of the coated scaffolds increased by more than 10% after immersion in SBF for 28 days, which suggest their potential bioactivity.

Author contributions

Research design: O. J. (leader), N. J. (contributor), K. S. (contributor), B. P. (contributor), A. B. (contributor), A. L. (contributor), A. L. (contributor), and R. L. (contributor); acquisition, analysis, or interpretation of data: O. J. (leader), N. J. (contributor), K. S. (contributor), B. P. (contributor); drafting the paper or revising it critically: O. J. (leader), N. J. (contributor), K. S. (contributor), B. P. (contributor); approval of the submitted and final versions: O. J. (leader).

Conflicts of interest

There are no conflicts to declare.

Acknowledgements

This research was financially supported by the Administrative and Management Unit for Enhancing the Competitiveness of the Country. Equipment support was provided by the Department of Materials Engineering, Faculty of Engineering, Kasetsart University. The authors thank Ms. Siraprapa Pitiphattharabun and Mr Krittin Auewattanapun for the valuable discussions and assistance.

Notes and references

1 T. Tariverdian, F. Sefat, M. Gelinsky and M. Mozafari, *Handbook of Tissue Engineering Scaffolds: Volume One*, Elsevier, 2019, pp. 189–209.
2 T. Ghassemi, A. Shahroodi, M. H. Ebrahimzadeh, A. Mousavian, J. Movaffagh and A. Moradi, *Arch. Bone Jt. Surg.*, 2018, **6**, 90–99.
3 T. M. De Witte, L. E. Fratila-Apachitei, A. A. Zadpoor and N. A. Peppas, *Regener. Biomater.*, 2018, **5**, 197–211.
4 B. N. Brown, J. E. Valentin, A. M. Stewart-Akers, G. P. McCabe and S. F. Badylak, *Biomaterials*, 2009, **30**, 1482–1491.
5 D. W. Hutmacher, *Biomaterials*, 2000, **21**, 2529–2543.
6 J. R. Porter, T. T. Ruckh and K. C. Popat, *Biotechnol. Prog.*, 2009, **25**, 1539–1560.
7 T. Kokubo, H.-M. Kim and M. Kawashita, *Biomaterials*, 2003, **24**, 2161–2175.
8 B. I. Oladapo, S. A. Zahedi and A. O. M. Adeoye, *Composites, Part B*, 2019, **158**, 428–436.
9 J. Kruger, *Int. Mater. Rev.*, 1988, **33**, 113–130.
10 S. P. Patterson, R. H. Daffner and R. A. Gallo, *Am. J. Roentgenol.*, 2005, **184**, 1219–1222.
11 C. Liu, P. Wan, L. L. Tan, K. Wang and K. Yang, *J. Orthop. Translat.*, 2014, **2**, 139–148.
12 R. Saidi, M. H. Fathi and H. Salimijazi, *Bull. Mater. Sci.*, 2015, **38**, 1367–1374.
13 N. Shayesteh Moghaddam, M. Taheri Andani, A. Amerinatanzi, C. Haberland, S. Huff, M. Miller, M. Elahinia and D. Dean, *Biomanuf. Rev.*, 2016, **1**, 1–16.
14 G. Eddy Jai Poinern, S. Brundavanam and D. Fawcett, *Am. J. Biomed. Eng.*, 2013, **2**, 218–240.
15 M. T. Andani, N. Shayesteh Moghaddam, C. Haberland, D. Dean, M. J. Miller and M. Elahinia, *Acta Biomater.*, 2014, **10**, 4058–4070.
16 J. A. McGeough, *The Engineering of Human Joint Replacements: McGeough/The Engineering*, John Wiley & Sons Ltd, Chichester, UK, 2013.
17 M. C. Bottino, P. G. Coelho, V. A. R. Henriques, O. Z. Higa, A. H. A. Bressiani and J. C. Bressiani, *J. Biomed. Mater. Res., Part A*, 2009, **88**, 689–696.
18 S. Sista, C. Wen, P. D. Hodgson and G. Pande, *Mater. Sci. Eng., C*, 2013, **33**, 1573–1582.

19 M. Niinomi, M. Nakai and J. Hieda, *Acta Biomater.*, 2012, **8**, 3888–3903.

20 D. D. Kiradzhiyska, Y. N. Feodorova, M. M. Draganov, Ch. A. Girginov, A. P. Viraneva, T. A. Yovcheva and R. D. Mantcheva, *AIP Conference Proceedings*, AIP Publishing LLC, Istanbul, Turkey, 2016.

21 K. Kisters, B. Winterberg, M. Barenbrock, M. Hausberg and K. H. Rahn, *Clin. Nephrol.*, 1999, **5**, 191–193.

22 T. V. Kolekar, N. D. Thorat, H. M. Yadav, V. T. Magalad, M. A. Shinde, S. S. Bandgar, J. H. Kim and G. L. Agawane, *Ceram. Int.*, 2016, **42**, 5304–5311.

23 C. Cox, J. A. Thornby, G. J. Gibbons, M. A. Williams and K. K. Mallick, *Mater. Sci. Eng., C*, 2015, **47**, 237–247.

24 G. A. Fielding, A. Bandyopadhyay and S. Bose, *Dent. Mater.*, 2012, **28**, 113–122.

25 M. Jaishankar, T. Tseten, N. Anbalagan, B. B. Mathew and K. N. Beeregowda, *Interdiscip. Toxicol.*, 2014, **7**, 60–72.

26 I. O. Igbokwe, E. Igwenagu and N. A. Igbokwe, *Interdiscip. Toxicol.*, 2019, **12**, 45–70.

27 X. Sun, Z. Cao, Q. Zhang, M. Li, L. Han and Y. Li, *Chem.-Biol. Interact.*, 2016, **244**, 9–15.

28 G. L. Klein, *Osteoporos. Sarcopenia*, 2019, **5**, 2–5.

29 C. S. Martinez, A. G. Escobar, J. A. Uranga-Ocio, F. M. Peçanha, D. V. Vassallo, C. Exley, M. Miguel and G. A. Wiggers, *Reprod. Toxicol.*, 2017, **73**, 128–141.

30 O. A. Taiwo, *J. Occup. Environ. Med.*, 2014, **56**, S71–S72.

31 Y. She, N. Wang, C. Chen, Y. Zhu, S. Xia, C. Hu and Y. Li, *Biol. Trace Elem. Res.*, 2012, **147**, 246–250.

32 H. Yu, J. Zhang, Q. Ji, K. Yu, P. Wang, M. Song, Z. Cao, X. Zhang and Y. Li, *Ecotoxicol. Environ. Saf.*, 2019, **173**, 131–141.

33 C. Exley, *Expert Rev. Neurother.*, 2014, **14**, 589–591.

34 C. Exley, G. Mamutse, O. Korchazhkina, E. Pye, S. Strekopytov, A. Polwart and C. Hawkins, *Mult. Scler. J.*, 2006, **12**, 533–540.

35 L. Tomljenovic and C. A. Shaw, *J. Inorg. Biochem.*, 2011, **105**, 1489–1499.

36 H. Zhou and J. Lee, *Acta Biomater.*, 2011, **7**, 2769–2781.

37 G. E. Poinern, R. K. Brundavanam, N. Mondinos and Z.-T. Jiang, *Ultrason. Sonochem.*, 2009, **16**, 469–474.

38 S. Samavedi, A. R. Whittington and A. S. Goldstein, *Acta Biomater.*, 2013, **9**, 8037–8045.

39 X. Pei, L. Ma, B. Zhang, J. Sun, Y. Sun, Y. Fan, Z. Gou, C. Zhou and X. Zhang, *Biofabrication*, 2017, **9**, 045008.

40 B. Zhang, H. Sun, L. Wu, L. Ma, F. Xing, Q. Kong, Y. Fan, C. Zhou and X. Zhang, *Bio-Des. Manuf.*, 2019, **2**, 161–171.

41 B. Ghiasi, Y. Sefidbakht, S. Mozaffari-Jovin, B. Gharehcheloo, M. Mehrarya, A. Khodadadi, M. Rezaei, S. O. Ranaei Siadat and V. Uskoković, *Drug Dev. Ind. Pharm.*, 2020, **46**, 1035–1062.

42 K. Fox, P. A. Tran and N. Tran, *ChemPhysChem*, 2012, **13**, 2495–2506.

43 H. Siddiqui, K. Pickering and M. Mucalo, *Materials*, 2018, **11**, 1813.

44 S. V. Dorozhkin, *Biomaterials*, 2010, **31**, 1465–1485.

45 J. Khotib, S. C. Cantika, S. Samirah and A. S. Budiatin, *Folia Med.*, 2019, **55**, 176–187.

46 W. S. W. Harun, R. I. M. Asri, A. B. Sulong, S. A. C. Ghani and Z. Ghazalli, *Hydroxyapatite - Advances in Composite Nanomaterials, Biomedical Applications and Its Technological Facets*, ed. J. Thirumalai, InTech, 2018, pp. 69–88.

47 Z. Zhang, M. F. Dunn, T. D. Xiao, A. P. Tomsia and E. Saiz, *MRS Proc.*, 2001, **703**, V7.5.

48 C. Shuai, W. Yang, P. Feng, S. Peng and H. Pan, *Bioact. Mater.*, 2021, **6**, 490–502.

49 C. Shuai, B. Peng, P. Feng, L. Yu, R. Lai and A. Min, *J. Adv. Res.*, 2022, **35**, 13–24.

50 I. R. Gibson, *Hydroxyapatite (Hap) for Biomedical Applications*, Elsevier, 2015, pp. 269–287.

51 S. Liu, K. Li and R. Hughes, *Ceram. Int.*, 2003, **29**, 875–881.

52 N. Choksi and H. Desai, *Int. J. Appl. Chem.*, 2017, **13**, 377–384.

53 M. S. Lopes, A. L. Jardini and R. M. Filho, *Chem. Eng. Trans.*, 2014, **38**, 331–336.

54 A. Gregor, E. Filová, M. Novák, J. Kronek, H. Chlup, M. Buzgo, V. Blahnová, V. Lukášová, M. Bartoš, A. Nečas and J. Hošek, *J. Biol. Eng.*, 2017, **11**, 31–33.

55 G. Wang and A. Li, *Chin. J. Chem. Eng.*, 2008, **16**, 929–933.

56 S. Yang, Z.-H. Wu, W. Yang and M.-B. Yang, *Polym. Test.*, 2008, **27**, 957–963.

57 T. T. Li, L. Ling, M.-C. Lin, Q. Jiang, Q. Lin, J.-H. Lin and C.-W. Lou, *J. Nanomater.*, 2019, **9**, 679.

58 M. C. Lin, C. W. Lou, J. Y. Lin, T. A. Lin, Y.-S. Chen and J. H. Lin, *Mater. Sci. Eng., C*, 2018, **91**, 404–413.

59 S. Uma Maheshwari, V. K. Samuel and N. Nagiah, *Ceram. Int.*, 2014, **40**, 8469–8477.

60 R. P. Pawar, S. U. Tekale, S. U. Shisodia, J. T. Totre and A. J. Domb, *Recent Pat. Regener. Med.*, 2014, **4**, 40–51.

61 D. da Silva, M. Kaduri, M. Poley, O. Adir, N. Krinsky, J. Shainsky-Roitman and A. Schroeder, *Chem. Eng. J.*, 2018, **340**, 9–14.

62 L. Wang, D. Barbieri, H. Zhou, J. D. de Bruijn, C. Bao and H. Yuan, *J. Biomed. Mater. Res., Part A*, 2015, **103**, 1919–1929.

63 Z. Shi, X. Huang, Y. Cai, R. Tang and D. Yang, *Acta Biomater.*, 2009, **5**, 338–345.

64 Q. Tian, J. Lin, L. Rivera-Castaneda, A. Tsanhani, Z. S. Dunn, A. Rodriguez, A. Aslani and H. Liu, *Sci. Rep.*, 2019, **9**, 1–27.

65 Q. Hu, Z. Tan, Y. Liu, J. Tao, Y. Cai, M. Zhang, H. Pan, X. Xu and R. Tang, *J. Mater. Chem.*, 2007, **17**, 4690–4698.

66 C. Rey, C. Combes, C. Drouet and H. Sfihi, *Adv. Sci. Technol. Res. J.*, 2006, **49**, 27–36.

67 G. Ciobanu, G. Carja, O. Ciobanu, I. Sandu and A. Sandu, *Micron*, 2009, **40**, 143–146.

68 L. Morejón, J. A. Delgado, A. A. Ribeiro, M. Varella de Oliveira, E. Mendizábal, I. García, A. Alfonso, P. Poh, M. van Griensven and E. R. Balmayor, *Int. J. Mol. Sci.*, 2019, **20**, 1790.

69 B. Leukers, H. Gülkan, S. H. Irsen, S. Milz, C. Tille, M. Schieker and H. Seitz, *J. Mater. Sci.: Mater. Med.*, 2005, **16**, 1121–1124.

70 Y. W. Won, A. N. Patel and D. A. Bull, *Biomaterials*, 2014, **35**, 5627–5635.

71 B. T. Smith, M. Santoro, E. C. Grosfeld, S. R. Shah, J. J. J. P. van den Beucken, J. A. Jansen and A. G. Mikos, *Acta Biomater.*, 2017, **50**, 68–77.

72 H. W. Kim, S.-Y. Lee, C.-J. Bae, Y.-J. Noh, H.-E. Kim, H.-M. Kim and J. S. Ko, *Biomaterials*, 2003, **24**, 3277–3284.

73 G. L. Converse, T. L. Conrad, C. H. Merrill and R. K. Roeder, *Acta Biomater.*, 2010, **6**, 856–863.

74 G. Schmidmaier, B. Wildemann, P. Schwabe, R. Stange, J. Hoffmann, N. P. Südkamp, N. P. Haas and M. Raschke, *J. Biomed. Mater. Res.*, 2002, **63**, 168–172.

75 P. Feng, P. Wu, C. Gao, Y. Yang, W. Guo, W. Yang and C. Shuai, *Adv. Sci.*, 2018, **5**, 1700817.

76 C. Feng, K. Zhang, R. He, G. Ding, M. Xia, X. Jin and C. Xie, *J. Adv. Ceram.*, 2020, **9**, 360–373.

77 C. Costa de Almeida, L. Á. Sena, M. Pinto, C. A. Muller, J. H. Cavalcanti Lima and G. de A. Soares, *Braz. Dent. J.*, 2005, **16**, 75–81.

78 P. N. Chavan, M. M. Bahir, R. U. Mene, M. P. Mahabole and R. S. Khairnar, *Mater. Sci. Eng., B*, 2010, **168**, 224–230.

79 P. Feng, S. Peng, C. Shuai, C. Gao, W. Yang, S. Bin and A. Min, *ACS Appl. Mater. Interfaces*, 2020, **12**, 46743–46755.

80 Y. W. Gu, K. A. Khor and P. Cheang, *Biomaterials*, 2004, **25**, 4127–4134.

81 V. Sarath Chandra, K. Elayaraja, R. V. Suganthi, M. I. Ahymah Joshy, I. Sulania, P. K. Kulriya, K. Asokan, D. Kanjilal and S. Narayana Kalkura, *Adv. Mater. Lett.*, 2013, **4**, 438–443.

82 A. Ito, K. Maekawa, S. Tsutsumi, F. Ikazaki and T. Tateishi, *J. Biomed. Mater. Res.*, 1997, **36**, 522–528.

83 Z. Yang, L. Xia and J. Han, *Adv. Biomed. Eng. Tech.*, 2015, **2**, 13–19.